

# FlowSteer: Conditioning Flow Field for Consistent Image Restoration

Tharindu Wickremasinghe<sup>1</sup>, Chenyang Qi<sup>2</sup>, Harshana Weligampola<sup>1</sup>, Zhengzhong Tu<sup>3</sup>, Stanley H. Chan<sup>1</sup>  
<sup>1</sup>Purdue University <sup>2</sup>HKUST <sup>3</sup>Texas A&M University

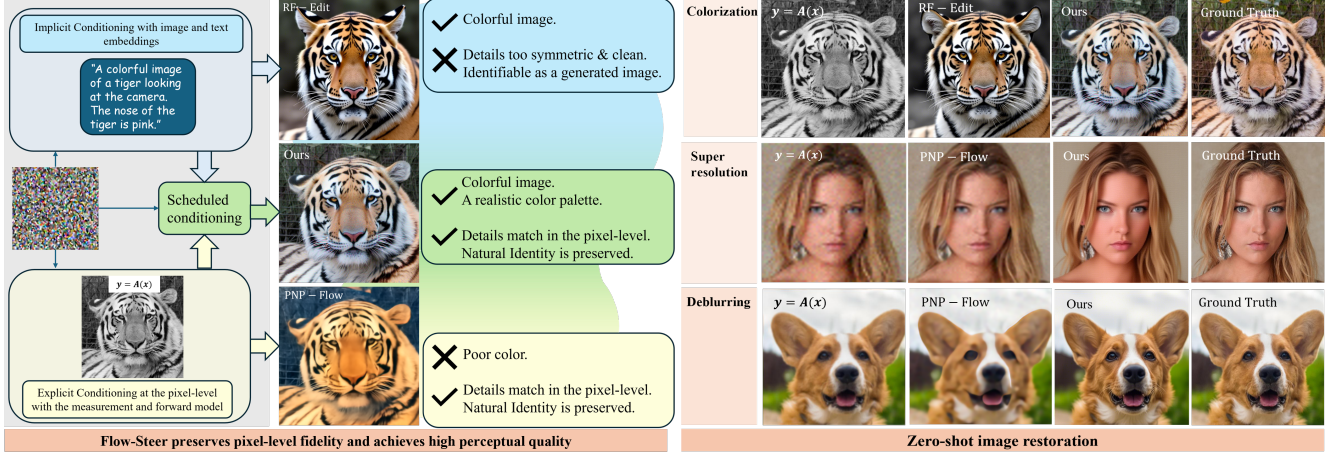


Figure 1. Left: FlowSteer estimates a clean image  $x$  from a measurement  $y$  generated by a degradation operator  $A$ . It achieves both **pixel-level fidelity by conditioning on the degradation model**, and **high perceptual quality utilizing prompt and attention guidance**. Right: FlowSteer demonstrates advantage on colorization, super-resolution and deblurring tasks in both fidelity and perceptual quality.

## Abstract

Flow-based text-to-image (T2I) models excel at prompt-driven image generation, but falter on Image Restoration (IR), often “drifting away” from being faithful to the measurement. Prior work mitigate this drift with data-specific flows or task-specific adapters that are computationally heavy and not scalable across tasks. This raises the question “Can’t we efficiently manipulate the existing generative capabilities of a flow model?” To this end, we introduce **FlowSteer (FS)**, an operator-aware conditioning scheme that injects measurement priors along the sampling path, coupling a frozen flow’s implicit guidance with explicit measurement constraints. Across super-resolution, deblurring, denoising, and colorization, FS improves measurement consistency and identity preservation in a strictly zero-shot setting—**no retrained models, no adapters**. We show how the nature of flow models and their sensitivities to noise inform the design of such a scheduler. FlowSteer, although simple, achieves a higher fidelity of reconstructed images, while leveraging the rich generative priors of flow models. All data and code will be public [here](#).

## 1. Introduction

Over the past few years, diffusion models have demonstrated impressive generative capability [21, 52], for many image editing [2, 18, 37, 56] and restoration tasks [9, 25, 46, 51]. Diffusion models, however, are known to have computational issues because one needs to run tens to hundreds of diffusion steps to obtain the result [12, 44, 50]. The more recently introduced flow models have shown initial success as an alternative to diffusion-based Text to Image (T2I) models, where they can generate images with higher perceptual quality and aesthetics [1, 45, 64]. However, flow models have not been widely adopted in image restoration tasks. If flow models are consistently faster and produce higher aesthetic quality, why are they not used in image restoration?

The biggest challenge of using a flow model for image restoration is the requirement for image fidelity. In image editing, the model can be more imaginative because the goal is not to preserve pixel-level fidelity [38, 55, 61, 63]. In image restoration, however, the forward image formation model provides a more restrictive constraint on what images are allowed to be generated. In theory, if a flow model is conditioned sufficiently, it is possible to obtain a restored image  $\hat{x}$  that has sufficient fidelity, such that  $y \approx A\hat{x}$ ,

where  $\mathbf{A}$  is the degradation formulation and  $\mathbf{y}$  is the measurement of degraded image. If this can be achieved, then we will have both superior generative restoration and be much faster than the diffusion counterparts.

More recent image editing methods use implicit conditioning methods with embedded features [37, 58, 60]. First, a degraded input image is inverted into a noisy latent through flow inversion. At each step, features from underlying Diffusion Transformers (DiTs) are cached as layout guidance [26, 27, 30]. The inverted latent is then denoised by a prompt-guided Flux [3, 31] model, with selected steps fusing the cached features back into the trajectory. This approach only guides the overall layout of the input image, without any explicit conditioning on the pixel-level fidelity. Therefore, the output images have high perceptual quality and visual appeal, but the identity of the subject is lost. On the other hand, explicit pixel-level conditioning has been attempted through PNP-Flow [36] in every step of the denoising path. As a result, it is prone to excessive blur artifacts, and cannot achieve the rich colors, sharp textures, and high perceptual quality achievable with the generative priors.

In this paper, we present a flow-based image restoration method by making a critical observation: In Flow-based image restoration, the forward model cannot be *uniformly* applied throughout the solution trajectory. Instead, we introduce a scheduler known as Flow-Steer(FS) to control the amount of forward model conditioning to be added to the solution trajectory. Specifically, no conditioning should be introduced in the beginning when the estimate is largely still in the latent space. Conditioning should be introduced toward the middle or latter stage of the solution trajectory when the estimate is becoming a meaningful image. Since Flow-Steer is a scheduler that can be added to any flow model, it offers a *training-free* zero-shot upgrade of the flow-based image restoration at nearly no additional cost. To demonstrate this, we adapt a flow-based inversion-reconstruction pipeline. Shared attention features provide implicit conditioning combined with text prompts, whereas the Flow Steer schedule offers pixel-level conditioning.

In summary, our main contributions are threefold:

1. We examine and explain the challenges of conditioning flow models towards pixel-level fidelity.
2. We propose Flow-Steer, a scheduler that aims to mitigate the challenges by telling the flow model when to include forward model conditioning.
3. We demonstrate that Flow-Steer is a universal scheme that can be adopted to a variety of image restoration tasks, including but not limited to deblurring, denoising, colorization, and super-resolution.

---

#### Algorithm 1 Fidelity update in a diffusion path [62]

---

```

1:  $\mathbf{x}_N \sim \mathcal{N}(\mathbf{0}, \mathbf{I})$ 
2: for  $t = N, \dots, 1$  do
3:    $\mathbf{x}_{0|t} \leftarrow \frac{1}{\sqrt{\bar{\alpha}_t}} (\mathbf{x}_t - \mathcal{Z}_\theta(\mathbf{x}_t, t) \sqrt{1 - \bar{\alpha}_t})$   $\triangleright$  denoise
4:    $\hat{\mathbf{x}}_{0|t} \leftarrow \mathbf{A}^\dagger \mathbf{y} + (\mathbf{I} - \mathbf{A}^\dagger \mathbf{A}) \mathbf{x}_{0|t}$   $\triangleright$  fidelity update
5:    $\mathbf{x}_{t-1} \sim \mathcal{N}(\mu_t(\mathbf{x}_t, \hat{\mathbf{x}}_{0|t}), \sigma_t^2 \mathbf{I})$   $\triangleright$  project back
6: end for
7: return  $\mathbf{x}_0$ 

```

---

## 2. Related Works

### 2.1. Image restoration with measurement fidelity

**Sampling diffusion paths.** Since the introduction of diffusion models [21, 39, 52, 53] for image generation, people have quickly realized these models can be used in image restoration. Diffusion-based image restoration models [7, 24, 25, 62] pioneered operator-aware restorations. Every sample along the reconstruction path can be conditioned to have fidelity towards a noise-free forward model  $\mathbf{y} = \mathbf{A}\mathbf{x}$  through a projection step. The core idea is to alternate between 1) a step in the direction of the log-likelihood  $\nabla_{\mathbf{x}} \log p(\mathbf{y}|\mathbf{x})$  for higher fidelity, and 2) a denoising step or a step towards the log-prior  $\nabla_{\mathbf{x}} \log p(\mathbf{x})$ . Algorithm 1 shows how the diffusion schedule of DDIM [52] was modified for image restoration through a  $\nabla_{\mathbf{x}} \log p(\mathbf{y}|\mathbf{x})$  step by DDNM. [62].

**More updates along the sampling path.** Various additional improvements to the sampling path were introduced since then. DiffPIR [68] wraps a plug-and-play style update [57] inside each step along the diffusion sampling path. DPS [9] extends the work beyond the linear model, and relaxes a strict-measurement consistency update. This allows non-linear and noisy inverse problems to be solved with diffusion priors. Recently, DPIR [29] shows that using the both text prompts and the degraded image improves the reconstruction quality. RDMD [59] suggests a linearly weighted sum between a stochastic generative sample and a deterministic update can improve the perception-distortion trade-off. All of the above improvements can be considered as a “scaffolding” to that of Algorithm 1.

### 2.2. Flow-based image editing and restoration

**Flow models.** Flow Matching (FM) [32] and Rectified Flow (RF) [34] reframed the generative modeling as learning velocity fields/ODE transports—aiming for linear sampling paths, fewer steps, and stronger quality [49]. Recent DiT/RF-Transformer systems [14, 48] scaled these ideas for Text to Image(T2I), making flow-style models much faster during inference. (e.g., SD3/DiT [54] and FLUX-style rectified-flow transformers [3]).

**Editing with rectified flows.** RF models perform much

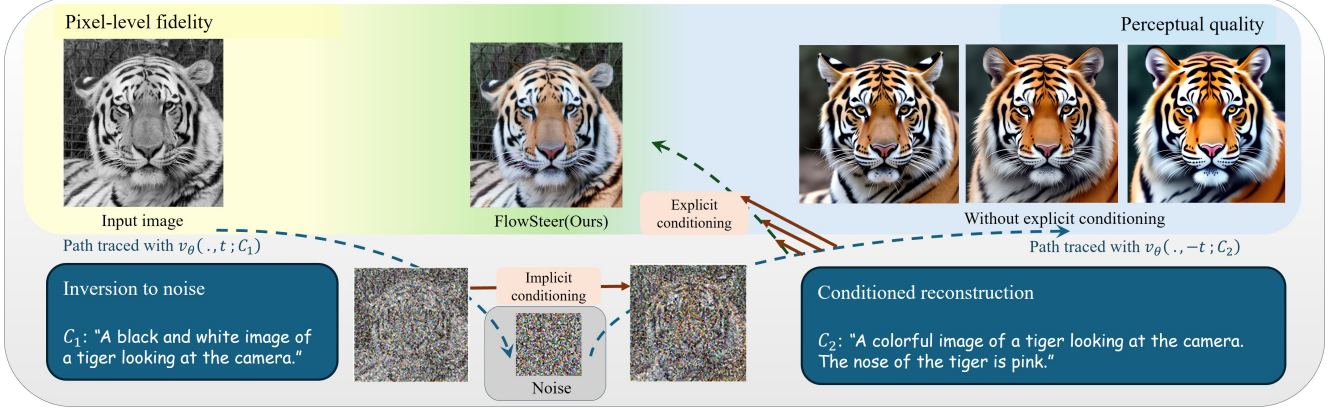


Figure 2. Image inversion(left) and reconstruction(right) paths of a flow model. A pre-trained flow trajectory  $v_\theta$  is conditioned implicitly by language prompts ( $C_1, C_2$ ) and feature sharing between paths. FlowSteer introduces an explicit conditioning schedule (center) to steer the reconstruction path toward high pixel-level fidelity without retraining the model.

better than their diffusion counterparts in image editing with T2I conditioning[10, 64]. RF-Edit [60] derives second-order samplers and share features between inversion and editing to reduce the drift. More work show fast, training-free inversion and editing in as few as 8 steps, and edit specific regions of an image [10, 11, 22, 45]. However, these flow models are not common in image restoration for they are unable to produce consistent images with high fidelity to a measurement.

**Flow models for restoration.** Works such as PnP-Flow [36], D-Flow [4], and Flow Priors [67] demonstrate that flow models can be used in several image restoration tasks. However, these require a flow model to be separately trained for *each* dataset. Thus, it is not transferrable to off-the shelf flow-based T2I models (such as flux [31]), and hence is not scalable.

In this paper we show that pre-trained flow models can, in fact, be used for a range of image restoration tasks in a truly zero-shot manner, *without* any retraining of the model. We find that flow models are sensitive to perturbations in conditioning, and that the conditioning using the forward model should introduced in middle or later stages of the reconstruction path.

### 3. Flow Models and Restoration

We review Rectified Flow models and conditioned generation. We then see how inversion and reconstruction have been conditioned for image editing and their inherent limitations. Finally, we look at how the data fidelity term could be explicitly conditioned in an ideal flow model.

#### 3.1. Rectified Flow models

Flow models are trained to map a clean image  $\mathbf{x}_0$  sampled from a clean distribution  $\pi_0$ , to a noise sample of the same

dimensionality,  $\mathbf{x}_1 \sim \pi_1$ . For Rectified Flows (RF), intermediate samples along the path are linear interpolations between  $\mathbf{x}_0$  and  $\mathbf{x}_1$ :

$$\mathbf{x}_t = t\mathbf{x}_0 + (1-t)\mathbf{x}_1, \quad t \in [0, 1]. \quad (1)$$

The training scheme is to learn a velocity field  $v_\theta(\cdot)$ , which is trained to predict the velocity between the two image distributions by minimizing

$$\min_{\theta} \int_0^1 \mathbb{E} \left[ \|\mathbf{x}_1 - \mathbf{x}_0 - v_\theta(\mathbf{x}_t, t)\|_2^2 \right] dt. \quad (2)$$

Given a sample of an intermediate image  $\mathbf{x}_t$  and the time index  $t \in (0, 1)$ , an ideally trained RF model should output the velocity that points to the desired clean image. For an incremental  $d\mathbf{x}_t$ , we can write  $d\mathbf{x}_t = v_\theta(\mathbf{x}_t, t)dt$ . Thereby, we have the Euler equation for solving the first-order ODE, implemented for a time schedule  $t = t_N, \dots, t_0$ :

$$\mathbf{x}_{t_{i-1}} = \mathbf{x}_{t_i} + (t_{i-1} - t_i) v_\theta(\mathbf{x}_{t_i}, t_i), \quad i \in \{N, \dots, 1\}. \quad (3)$$

Assuming an ideal model  $v_\theta$  that accurately estimates the velocity field conditioned on a text prompt  $C$  and timestep  $t$ , Classifier-Free Guidance[20] is further utilized to control the trajectory’s drift  $d\mathbf{x}_t$ , to align with the target attributes specified by  $C$ .

#### 3.2. Image Inversion and Reconstruction

Given an input measurement  $\mathbf{y}$  with degradation, the image editing framework first inverts it to a noise distribution  $\pi_1$ . In each step of inversion, the velocity field  $v_\theta(\cdot, t; C_1)$  is conditioned on a description  $C_1$  of the degraded image. (See Figure 2, left). Additionally, the attention maps at each step are cached to be fused with the reconstruction path.

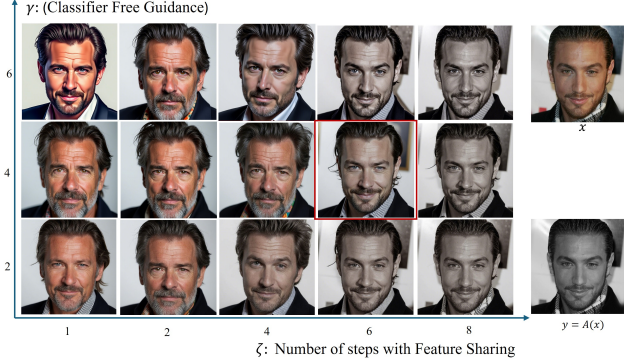


Figure 3. Effect of varying classifier-free guidance  $\gamma$  and feature-sharing steps  $\zeta$  on restoration quality. Increasing  $\gamma$  enhances color saturation but reduces fidelity to the measurement  $y$ , while increasing  $\zeta$  improves pixel-level consistency without recovering true color.

Next, the inverted latent is denoised by sampling  $v_\theta(\cdot, -t; C_2)$ , which is conditioned on a prompt  $C_2$  that describes the target image. As illustrated on the right of Figure 2, the discrete sampling steps formulate a trajectory from noise to clean image, where the cached attention maps are fused in the corresponding step. While this process steers the reconstruction toward a general manifold of high perceptual quality, the fidelity achieved by this standard inversion-and-reconstruction approach is insufficient for precise, high-quality image restoration.

### 3.3. Limitations of Implicit Conditioning

Fusing attention features from the inversion path into the reconstruction paths has its limitations. Most pre-trained flow models such as Flux [31] are trained in an encoded feature space mapped by VAE autoencoders [28, 44]. Thus, the entire flow algorithm runs on this embedding space, rather than in the pixel space. An attention map is a similarity of the tokens generated by  $2 \times 2$  patches on these VAE embeddings, which is compressed from the pixel space (e.g, Flux uses  $16 \times$ ). Thus, fusing attention features only preserves coarse-level details without guidance on low-level texture within each token. Furthermore, these coarse features are not decoupled, and we cannot separate out the unwanted artifacts. Consider the example shown in figure 3. Having many steps ( $\zeta$ ) that copy features from the inversion path tends to copy unwanted artifacts, leading the results to have a black-and-white color palette after reconstruction.

The other parameter used widely is the Classifier-Free Guidance (CFG) [20] parameter that controls the generative hallucinations of the flow model. This parameter  $\gamma$  has to be tuned together with  $\zeta$ . Notice that even the best configuration of  $(\gamma, \zeta)$ , gives an image lacking in pixel-level fidelity. This motivates the explicit use of measurement  $y$  and the

### Algorithm 2 Enforcing fidelity into an ideal flow path

---

```

1:  $\hat{\mathbf{x}}_N \sim \pi_1 = \mathcal{N}(\mathbf{0}, \mathbf{I})$ 
2:  $C \leftarrow$  "A colorful image of a tiger..."
3: for  $i = N, \dots, 1$  do
4:    $\hat{\mathbf{x}}_{t_i} = \hat{\mathbf{x}}_{t_{i+1}} + v_\theta(\hat{\mathbf{x}}_{t_{i+1}}, t_i; C)(t_{i+1} - t_i)$ 
5:    $\hat{\mathbf{x}}_{0|t_i} = \frac{1}{(1-t_i)+\epsilon} \hat{\mathbf{x}}_{t_i} - \frac{t_i}{(1-t_i)+\epsilon} \eta$   $\triangleright$  denoise
6:    $\bar{\mathbf{x}}_{0|t_i} \leftarrow \mathbf{A}^\dagger \mathbf{y} + (\mathbf{I} - \mathbf{A}^\dagger \mathbf{A}) \hat{\mathbf{x}}_{0|t_i}$   $\triangleright$  fidelity update
7:    $\hat{\mathbf{x}}_{t_i} = (1 - t_i) \bar{\mathbf{x}}_{0|t_i} + t_i \eta$   $\triangleright$  project back
8: end for
9: return  $\mathbf{x}_0$ 

```

---

degradation operator  $\mathbf{A}$  for an explicit guidance towards the high fidelity region.

### 3.4. Explicit Conditioning for Ideal Flows

Assuming a linear forward model  $\mathbf{y} = \mathbf{A}\mathbf{x}$  is known, we can attempt for pixel level fidelity by adapting the ideas presented in section 2.1 by explicitly enforcing  $\mathbf{A}\bar{\mathbf{x}}_{0|t_i} = \mathbf{y}$  as outlined in algorithm 2.

Suppose that at a time  $t + 1$  in the reconstruction path, we have a prediction for  $\mathbf{x}_{t+1}$ . This is line 4 in algorithm 2. To match with the framework of the null-space update in algorithm 1, we need to follow the forward model path defined for  $v_\theta(\cdot)$  to predict  $\hat{\mathbf{x}}_{0|t}$ . This is the denoising step (Step 3) of the algorithm 1, which can be adapted for flow using the forward model equation 1. Assuming an ideally behaving flow model, the intermediate  $\mathbf{x}_{t_i}$  lies in the linearly interpolated position  $\hat{\mathbf{x}}_{t_i} = t_i \mathbf{x}_1 + (1 - t_i) \hat{\mathbf{x}}_0$ .

Taking  $\mathbf{x}_1$  to be Gaussian noise  $\eta \sim \mathcal{N}(\mathbf{0}, \mathbf{I})$ , we get  $\hat{\mathbf{x}}_{0|t_i} = \frac{1}{(1-t_i)+\epsilon} \hat{\mathbf{x}}_{t_i} - \frac{t_i}{(1-t_i)+\epsilon} \eta$ . Notice how this can be interpreted as a denoising step  $\hat{\mathbf{x}}_{0|t} \leftarrow D(\hat{\mathbf{x}}_t)$ . Next, the predicted clean image is updated in the null-space, followed by a re-projection back onto the intermediate step  $t_i$ .

Note that this analysis is valid if we have access to an ideal flow model  $v_\theta$ . Even with such a model, we require the  $\epsilon$  term in the denominators during implementation for numerical stability.

## 4. Steering Rectified Flows in the Wild

### 4.1. Fragile, non-ideal flow models

**Flow models are sensitive to noise.** Unlike diffusion models, flow models are not trained with a  $\sigma_t$  schedule, and have no inherent "buffer" for randomness in each step  $t$ . However, the following sources of noise  $\eta$  are inevitable:

1. No RF model will predict the true velocity in every time step. Thus  $v_\theta(\hat{\mathbf{x}}_{t_{i+1}}, t_i) = v_{ideal}(\theta(\hat{\mathbf{x}}_{t_{i+1}}, t_i)) + \eta_1$  and  $\mathbf{x}_{t_i} = \mathbf{x}_{t_i}^{ideal} + \Delta t \eta_1$
2. The forward and backward operators from  $\mathbf{A}$  may not be fully accurate. For example, for colorization and super-resolution, the pseudo-inverse operator  $\mathbf{A}^\dagger$  is not exact. Hence  $\hat{\mathbf{x}}_{t_i} \leftarrow \mathbf{A}^\dagger \mathbf{y} + (\mathbf{I} - \mathbf{A}^\dagger \mathbf{A}) \hat{\mathbf{x}}_{t_i} + \eta_2$

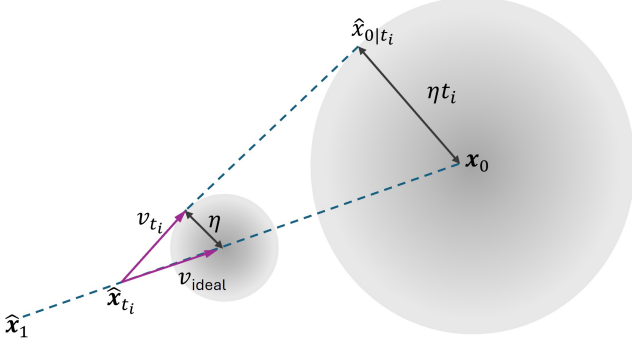


Figure 4. Linear projections of flow models exacerbate the errors from non-ideal velocities. We recommend to avoid projection operations to estimate  $\hat{\mathbf{x}}_{0|t_i}$  when  $t_i \approx 1$ .

3. RF models are trained in an embedding space through autoencoders. These embeddings need to be converted back to a pixel space before the pixel-level fidelity is conditioned.

The above sources of inherent randomness, added to numerical/precision errors, create a random noise at each step that we choose to enforce fidelity. Suppose that noise is characterized by a standard deviation  $\eta_{\text{effective}}$ . In diffusion models, the training scheme inherently has a random noise schedule  $\sigma_t$ . Therefore, as long as the hyper-parameters ensure  $\eta_{\text{effective}} \ll \sigma_t$ , such fidelity updates at every step do not pose problems. In contrast, since the training scheme of flow models does not account for such randomness (see equation 1), even a well-trained flow model with powerful priors cannot converge to desirable images with such noise-inducing fidelity updates on each step. This is the reason for the fragility of using Diffusion-style updates on flow models, and we posit that this is a key challenge in the research community to adapt flow models for image restoration.

## 4.2. Steering the Flow

As we shall see, there are some practical assumptions that will lead us to a schedule where an explicit update would not divert the flow unnecessarily. The only adjustment required is a parameter scheduler  $\{\lambda_i\}$ , to achieve the explicit conditioning that we expected from Algorithm 2. Some practical decisions that lead to this scheduler are as follows:

### Avoid conditioning early on in the reconstruction.

Note that as a consequence of the non-ideal nature of the flow models, the noise gets scaled by a factor of  $\Delta t$ , and the estimation error for  $\hat{\mathbf{x}}_{0|t_i}$  scales by  $t_i$ . A high-level view of this is shown in Figure 4.

**Avoid projecting to and from  $\hat{\mathbf{x}}_{0|t}$ .** When  $t_i$  is close to 0, we can approximate the denoise step of algorithm 2 to be  $\hat{\mathbf{x}}_{0|t_i} \approx \hat{\mathbf{x}}_{t_i}$ . This avoids linearly projecting to find an approximate  $\mathbf{x}_{0|t_i}$ . This results in the fidelity update enforcing  $\mathbf{A}\hat{\mathbf{x}}_t \equiv \mathbf{y}$  at the steps  $t_i$  that we decide to condition the flow.

---

### Algorithm 3 FlowSteer: for a Non-ideal Flow model

---

```

1:  $\hat{\mathbf{z}}_N \sim \pi_1 = \mathcal{N}(\mathbf{0}, \mathbf{I})$ 
2:  $C \leftarrow$  "A colorful image of a tiger..."
3: for  $i = N, \dots, 1$  do
4:    $\hat{\mathbf{z}}_{t_i} = \hat{\mathbf{z}}_{t_{i+1}} + v_\theta(\hat{\mathbf{z}}_{t_{i+1}}, t_i; C)(t_{i+1} - t_i)$ 
5:    $\hat{\mathbf{x}}_{t_i} = \text{Decoder}(\hat{\mathbf{z}}_{t_i})$ 
6:   if  $\lambda_i > 0$ :
7:      $\hat{\mathbf{x}}_{t_i} \leftarrow \mathbf{A}^\dagger \mathbf{y} + \lambda_i (\mathbf{I} - \mathbf{A}^\dagger \mathbf{A}) \hat{\mathbf{x}}_{t_i} \triangleright$  fidelity update
8:    $\hat{\mathbf{z}}_{t_i} = \text{Encoder}(\hat{\mathbf{x}}_{t_i})$ 
9: end for
10: return  $\text{Decoder}(\mathbf{z}_0)$ 
```

---

This is a strict constraint to follow on each step, and makes intuitive sense:  $\mathbf{y} = \mathbf{A}\hat{\mathbf{x}}_t = \mathbf{A}\hat{\mathbf{x}}_0$  when  $\mathbf{x}_t \simeq \mathbf{x}_0$ .

Therefore, we should avoid steps 5 and 7 in algorithm 2, and wait until  $t_i$  is closer to 0. One could also intuitively see from figure 4, that with such noise sensitivity, we should avoid more noise-inducing linear projections until necessary. Our ablations further validate these recommendations.

## 4.3. A sparse update scheduler

The above two suggestions lead us to design a scheduler that decides which steps during the reconstruction path, which enforces  $\mathbf{A}\hat{\mathbf{x}}_{t_i} \equiv \mathbf{y}$ , achieve desirable fidelity. To control this, we propose using the fidelity update step with a sparse parameter schedule  $\{\lambda_i\}$ , for which the fidelity update triggers only if  $\lambda_i > 0$ . Furthermore, since available RF models operate in an embedding space, a Decoder-Encoder wrapper is needed to convert these embeddings into pixel space. The complete procedure is summarized in Algorithm 3.

## 4.4. Our baseline flow model and schedule recommendations

**The restoration pipeline.** We first convert our input image into a latent space using the ViT autoencoders. These latents are inverted into a noisy latent distribution through flow inversion, and we cache the attention map during inversion as layout guidance. Then, the inverted latent is denoised with multi-step inference of the Flux model. Our SteerFlow schedule decides the steps in which we merge both the layout guidance from the attention map and pixel-wise guidance from the degraded prior. In these steps, the latents are decoded back to image space, and the fidelity update is performed.

**The flow model.** We select the Flux-dev model [31] as our pre-trained RF model, with inversion and reconstruction paths having  $N = 30$  steps each. We then design our image inversion and reconstruction pipeline as described in section 3.2. For each input image, an input caption  $C_1$  describes the image with its degradation, and the target caption  $C_2$  describes the ideally restored image. We cache the attention maps of each inversion step for copying in the recon-

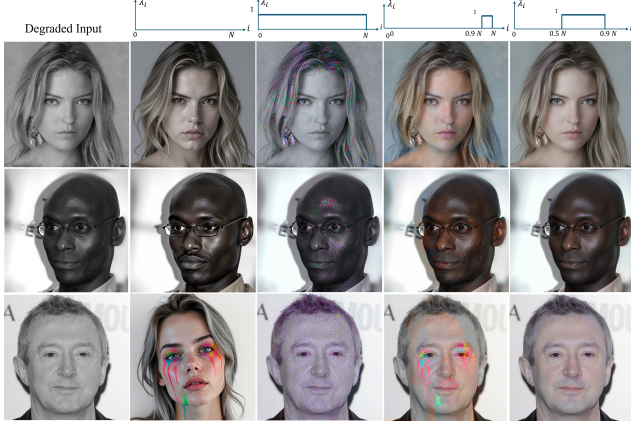


Figure 5. Colorizing with different  $\{\lambda_i\}$  schedules on our baseline RF model. No explicit conditioning creates hallucinations and loses identity. Having a constant conditioning with  $\lambda = 1$  introduces undesired noise.

struction path, specified by  $\zeta$ . The hyperparameters  $\gamma$  and  $\zeta$  (as described in Section 3.3) are chosen so that the best-available trade-off between fidelity and perceptual quality is obtained, and is kept at (4, 4) for all experiments. This forms our implicit conditioning scheme, on top of which FlowSteer is applied.

**FlowSteer scheduler.** To improve fidelity and explicitly condition the forward model, we design the FS scheduler  $\{\lambda_i\}$  so that a set of validation images achieves a desirable trade-off between fidelity and reconstruction quality. At its simplest form, the schedule will be a rectangular window, with three parameters  $i_{\text{start}}, i_{\text{stop}}, h$  defining the schedule:

$$\lambda_i = \begin{cases} h & \text{if } i_{\text{start}} \leq i \leq i_{\text{stop}}, \\ 0 & \text{otherwise.} \end{cases} \quad (4)$$

**Schedule recommendations.** In general, we recommend that the schedule start enforcing fidelity between 50%-90% of the total steps. The intuition for this is based on how image generation proceeds from coarse to fine details along the reconstruction path, as discussed in recent work [18, 40, 47]. In the early steps, the color palette is formed, and the foreground and background are separated. Towards the end, finer details and textures are formed. Conditioning too late towards the end risks unwanted hallucinations. Conditioning too early introduces a higher effective noise (as described in Section 4.2) and directs the restoration toward a noisy output. Depending on the reconstruction task,  $(i_{\text{start}}, i_{\text{stop}})$  can be further fine-tuned for improved performance. The relative strength of the fidelity update can also be controlled by  $h$  to mitigate unwanted artifacts from the noisy conditioning step. Refer to ablations in Section 5.3 for the effects of  $(i_{\text{start}}, i_{\text{stop}})$  and other alternatives.

## 5. Experiments

In this section we evaluate FlowSteer on image restoration tasks. Section 5.1 presents implementation details, Section 5.2 compares our framework with other comparable methods, and Section 5.3 discusses ablation studies.

### 5.1. Implementation details

**Forward models.** We select the restoration tasks: colorization, denoising, deblurring, and 4x super resolution. Each forward model is modeled as an operator  $\mathbf{A}$ , and assigned a pseudo-inverse operator  $\mathbf{A}^\dagger$  to implement algorithm 3. Linear transforms are assumed following Wang *et al.* [62] for colorization and super resolution. For Deblurring, we follow Martin *et al.* [36] with a  $61 \times 61$ -pixel gaussian kernel with blur  $\sigma_b = 3.0$  for  $\mathbf{A}$ . A Wiener deconvolution operator [16, 17] with  $\Lambda_{\text{Wiener}} = 0.1$  is used for  $\mathbf{A}^\dagger$ . For denoising, the forward model is an additive Gaussian noise of  $\sigma_g = 0.2$ , and we set  $\mathbf{A} = \mathbf{A}^\dagger = \mathbf{I}$  for the fidelity update. We refer to the supplementary for more details.

**Data and metrics.** A set of 100 sampled images from AFHQ [8], CelebAHQ [23, 35] data is selected as our test data. A sample of 20 images from the same source is the validation split to tune hyper-parameters and run ablations. This forms a collection of human faces, pets, and wild animals. Our evaluation focuses on pixel-level fidelity and perceptual quality. PSNR, SSIM metrics measure the fidelity/ the consistency of the generated image to the forward model. To report the perceptual similarity between the predicted and ground truth images, we use LPIPS [65] and the Cosine similarity between CLIP [43] embeddings. For Colorization, we first implement a histogram matching algorithm for each color channel to ensure that global effects such as brightness, saturation shifts, and contrast doesn't effect the metrics.

### 5.2. Comparisons

We compare the restoration capability of FlowSteer with other flow models: OT-ODE [41], D-Flow [4], Flow-Priors [67], and PNP-Flow [36]. These methods induce a fidelity update in each step and, therefore, result in higher artifacts in the final restoration. To reproduce PNP-Flow [36], we use the separate flow models for humans and animals as provided by the authors. However, for our method, we use *the same flux model for all types of data*, and show that a large pretrained T2I model, such as Flux, can be steered for faithful image restoration.

Since models with an inversion-reconstruction pipeline have not been used for image restoration, we reproduce RF-Edit [60], tune the corresponding  $(\gamma, \zeta)$  parameters through a grid-search, and keep them constant throughout the test data. This baseline demonstrates that implicit conditioning loses the identity of the image, and that FlowSteer can

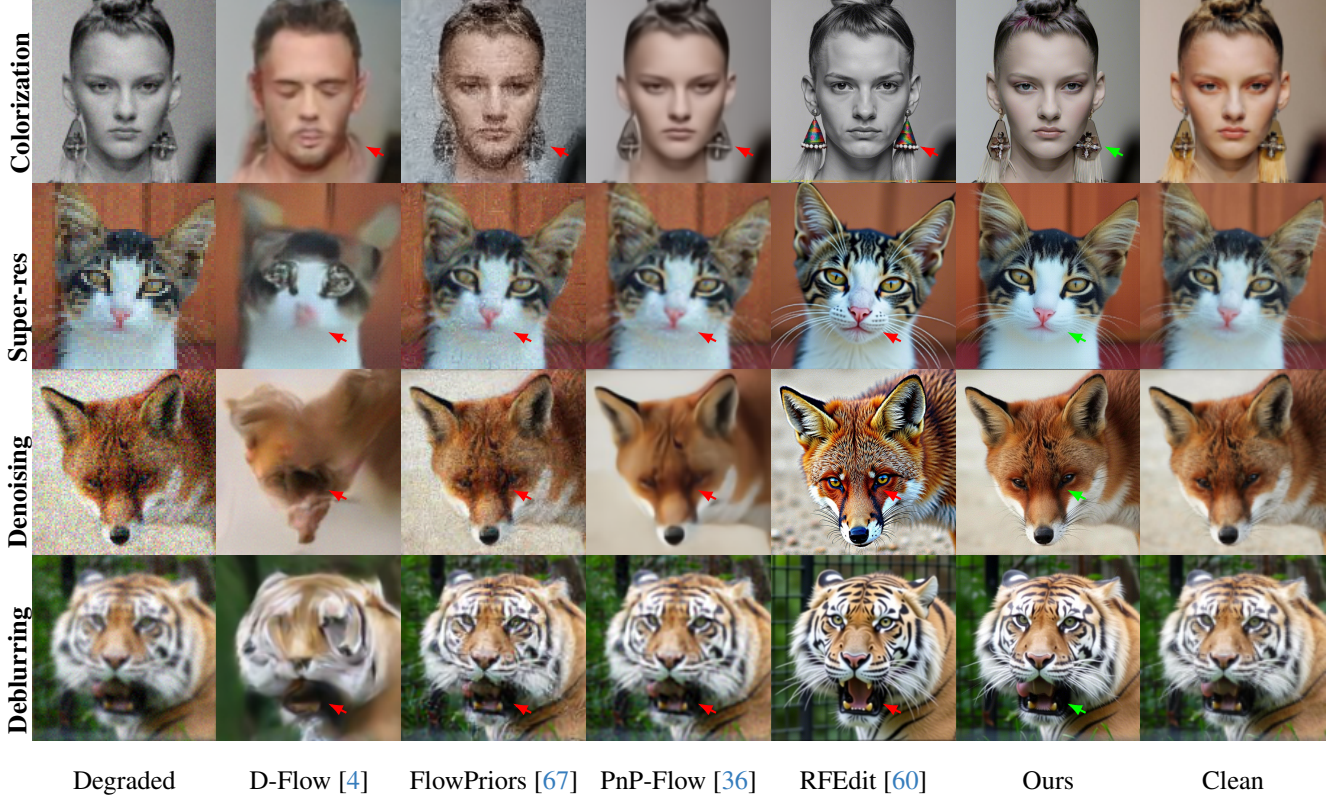


Figure 6. Qualitative comparison of flow-based methods. Columns 2-4 are image restoration models, and column 5 is an image editing model. The rows show four degradations: tasks focused on information reconstruction (colorization and  $4\times$  super-resolution) and tasks focused on corruption removal (denoising and deblurring). SteerFlow removes degradations, and details are generated without losing the identity of the subject.

achieve high pixel-level fidelity while maintaining a high visual quality.

**Fidelity and Perceptual quality.** FlowSteer preserves the perceptual qualities of the pre-trained T2I flux model (such as rich colors, fine details, and textures), while also achieving a high pixel-level fidelity with the degraded measurement. It enhances degraded details, without losing the identity of the subject. In the qualitative results of Figure 6, we see that characteristic facial features, whiskers, teeth, fur ...etc are enhanced, without changing the identity of the subject. This is reflected quantitatively in Table 1.

### 5.3. Ablations.

**The effect of  $\{\lambda_t\}$ .** We experimentally validate our practical design choices outlined in section 4.2. Having a continuous conditioning with  $\lambda = 1$  at every step introduces a noise that is only exacerbated as more steps are taken by the flow model. Our ablations (Figure 5) verify that explicit conditioning should generally be done at the middle of the schedule. The parameters  $(i_{\text{start}}, i_{\text{end}}, h)$  may be further tuned for better reconstructions.

**Complex schedules.**  $\{\lambda_i\}$  can be tuned for each task

separately, achieving better reconstruction scores. In table 2 we show the parameters of a two-step window, which has an additional parameter  $i_{\text{step}}$ , which indicates the step that changes the conditioning strength  $\lambda_i$  from  $h_1$  to  $h_2$ . Although more complex schedules can be designed, our results of table 1 are based on this two-step schedule.

**Avoiding projections to  $\hat{\mathbf{x}}_{0|t_i}$ .** In Section 4.2 we recommend to avoid the linear projection steps  $\hat{\mathbf{x}}_{0|t_i} \leftarrow \hat{\mathbf{x}}_{t_i}$ . This claim is experimentally verified in table 3 and figure 7. Note the remaining noise of the final reconstructions. The flow model is not trained with a noise schedule  $\sigma_t$  in each step. Thus, it conflates noise artifacts with necessary textures, and suggests a velocity update that highlights these unwanted artifacts.

**The Diffusion counterpart.** We compare Flowsteer with DDNM [62], which implements algorithm 1 on a pre-trained guided-diffusion network [12]. We observe that FlowSteer performs better owing to the powerful generative priors of the flux model. The implementation of the DDNM takes 100 steps on the reconstruction path [13], while SteerFlow samples the flux model  $N = 30$  steps for each reconstruction task.

Methods	Colorization				Super resolution				Deblurring				Denoising			
	PSNR $\uparrow$	SSIM $\uparrow$	LPIPS $\downarrow$	CLIP $\uparrow$	PSNR $\uparrow$	SSIM $\uparrow$	LPIPS $\downarrow$	CLIP $\uparrow$	PSNR $\uparrow$	SSIM $\uparrow$	LPIPS $\downarrow$	CLIP $\uparrow$	PSNR $\uparrow$	SSIM $\uparrow$	LPIPS $\downarrow$	CLIP $\uparrow$
<i>Reference</i>	27.1891	0.8333	0.2334	0.5807	26.7337	0.7829	0.2381	0.4380	28.2371	0.7586	0.2821	0.3095	22.7706	0.4399	0.4427	0.3178
D-Flow [4]	18.5295	0.5554	0.4977	0.2724	23.4039	0.6236	0.4132	0.2984	22.2396	0.6316	0.4104	0.2798	19.0651	0.5232	0.4840	0.2451
OT-ODE [41]			N/A		29.1072	0.8296	0.1994	0.6033	31.0467	0.8612	0.1984	0.5908	28.8276	0.8123	0.2505	0.4416
Flow-Priors [67]	21.7889	0.5716	0.4639	0.4808	27.6858	0.7151	0.3036	0.4724	30.4326	0.8350	0.2264	0.5535	28.8047	0.7645	0.2770	0.4479
PnP-flow [36]	27.1620	0.8640	0.2830	0.3482	31.2073	0.8753	0.1755	0.3938	32.7392	0.8840	0.1728	0.4597	30.5899	0.8733	0.2207	0.5103
RfEdit [60]	20.3255	0.6602	0.3648	0.8703	22.3243	0.7362	0.2822	0.7863	22.9813	0.7431	0.2750	0.7914	17.0219	0.4438	0.4545	0.8570
Ours	27.4214	0.8696	0.2081	0.7734	32.8552	0.9022	0.1700	0.6714	32.8749	0.9052	0.1486	0.8177	32.2125	0.8924	0.1822	0.7679

Table 1. Quantitative comparison with flow-based restoration methods. *Reference* uses the degraded image  $y$ . FlowSteer has high perceptual quality, and high pixel-level fidelity. We highlight the **best** and **second-best** per metric.

Degradation	General schedule setting			Fine-tuned schedule setting per task		
	Params ( $i_{\text{start}}, i_{\text{end}}, h$ )	PSNR $\uparrow$	LPIPS $\downarrow$	Params ( $i_{\text{start}}, i_{\text{step}}, i_{\text{end}}, h_1, h_2$ )	PSNR $\uparrow$	LPIPS $\downarrow$
Colorization	(0.5N, 0.9N, 1)	22.5841	0.3065	(0.4N, 0.50N, 0.95N, 1, 0.3)	<b>27.4214</b>	<b>0.2081</b>
Super-resolution	(0.5N, 0.9N, 1)	22.8262	0.3753	(0.5N, 0.70N, 0.85N, 1, 0.5)	<b>32.8552</b>	<b>0.1700</b>
Deblurring	(0.5N, 0.9N, 1)	23.1362	0.3959	(0.7N, 0.80N, 0.90N, 1, 0.3)	<b>32.8749</b>	<b>0.1486</b>
Denoising	(0.5N, 0.9N, 1)	22.4335	0.4677	(0.5N, 0.75N, 0.95N, 1, 0.5)	<b>30.3822</b>	<b>0.2313</b>

Table 2. Comparison of general and fine-tuned FlowSteer schedule settings across degradation tasks.

Degradation	with $\hat{x}_{0 t} \leftarrow \hat{x}_t$		w/o $\hat{x}_{0 t} \leftarrow \hat{x}_t$	
	PSNR $\uparrow$	LPIPS $\downarrow$	PSNR $\uparrow$	LPIPS $\downarrow$
Colorization	11.8157	0.6256	<b>27.4214</b>	<b>0.2081</b>
Super-resolution	12.0936	0.6168	<b>32.8552</b>	<b>0.1700</b>
Deblurring	12.1171	0.6228	<b>32.8749</b>	<b>0.1486</b>
Denoising	12.1006	0.6467	<b>30.3822</b>	<b>0.2313</b>

Table 3. Comparison of results with and without projection to  $\hat{x}_{0|t}$  in the fidelity step. Direct projection introduces additional noise that remains in image textures, leading to lower PSNR and higher LPIPS.

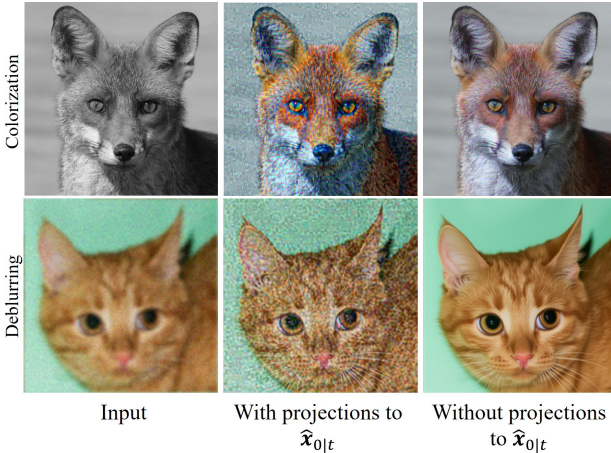


Figure 7. Reconstructed images with and without projecting to  $\hat{x}_{0|t}$  in the fidelity update step. Projections induce residual noise that persists in the reconstructed images.

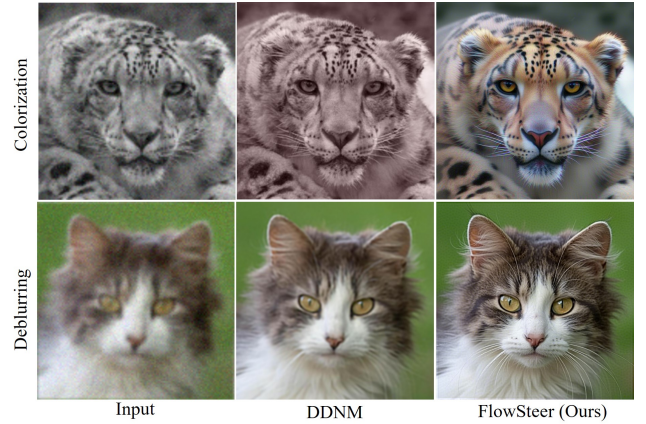


Figure 8. FlowSteer(30 steps) vs DDNM [62], which implements algorithm 1 on guided-diffusion [13] (100 steps).

## 6. Conclusion

Integrating flow-based T2I models into image restoration remains an open problem despite their efficiency over diffusion. FlowSteer articulates this challenge by enabling flow models to better respect the physical forward image formation model. By introducing a simple, yet effective scheduler during the inference process, FlowSteer ensures that the image restoration task will move along a trajectory that will lead to a physically consistent image. More importantly, FlowSteer is training-free, and can be applied to any existing flow-based T2I framework. Across multiple applications, including colorization, super-resolution, deblurring, and denoising, FlowSteer demonstrates both superior pixel-level fidelity and visual quality.

# FlowSteer: Conditioning Flow Field for Consistent Image Restoration

## Supplementary Material

### 7. Noise Sensitivity of the Flow Model

In Section 3, we describe that the flow model is sensitive to noisy intermediate projections. This raises the question: “Are there noise-robust algorithms from diffusion models, that can be reinterpreted for the flow-model scheme?” To the best of our knowledge, there are no such algorithms that can be directly translated to the flow scheme. The main reason is that a diffusion model is trained with a noise schedule  $\{\sigma_t\}$  for the time schedule  $t = t_N, \dots, t_0$ . This acts as an inherent buffer of randomness at each step, and is used to design a weight  $\lambda_t$  in fidelity update steps. To illustrate this, we present the robust version of Algorithm 1 noise and describe why it cannot be applied directly to the flow model.

#### 7.1. Noise-robust fidelity update with diffusion

**Fidelity update step.** Assume a linear forward model with additive noise  $\mathbf{y} = \mathbf{A}\mathbf{x} + \boldsymbol{\eta}$ ,  $\boldsymbol{\eta} \sim \mathcal{N}(\mathbf{0}, \sigma_y^2 \mathbf{I})$ . The DDNM-style fidelity update[62] for a noisy measurement would update line 4 in Algorithm 1 as follows.

$$\begin{aligned}\widehat{\mathbf{x}}_{0|t} &= \mathbf{A}^\dagger \mathbf{y} + (\mathbf{I} - \mathbf{A}^\dagger \mathbf{A}) \mathbf{x}_{0|t} \\ &= \mathbf{A}^\dagger (\mathbf{A}\mathbf{x} + \boldsymbol{\eta}) + (\mathbf{I} - \mathbf{A}^\dagger \mathbf{A}) \mathbf{x}_{0|t} \\ &= \mathbf{x}_{0|t} - \mathbf{A}^\dagger (\mathbf{A}\mathbf{x}_{0|t} - \mathbf{y}) + \mathbf{A}^\dagger \boldsymbol{\eta}, \quad \boldsymbol{\eta} \sim \mathcal{N}(\mathbf{0}, \sigma_y^2 \mathbf{I}),\end{aligned}\tag{5}$$

which makes explicit the extra noise term  $\mathbf{A}^\dagger \boldsymbol{\eta}$ .

**Projection back/ Posterior sampling step.** As in DDPM [21] or DDIM [52], a diffusion model samples/project back to the reconstruction path at time step  $t - 1$ . This is line 5 of Algorithm 1:

$$\mathbf{x}_{t-1} \sim \mathcal{N}(\boldsymbol{\mu}_t(\mathbf{x}_t, \widehat{\mathbf{x}}_{0|t}), \sigma_t^2 \mathbf{I}).$$

With the re-parametrization trick,

$$\mathbf{x}_{t-1} = \boldsymbol{\mu}_t(\mathbf{x}_t, \widehat{\mathbf{x}}_{0|t}) + \sigma_t \boldsymbol{\epsilon}_t, \quad \boldsymbol{\epsilon}_t \sim \mathcal{N}(\mathbf{0}, \mathbf{I}).\tag{6}$$

The posterior mean above is

$$\boldsymbol{\mu}_t(\mathbf{x}_t, \widehat{\mathbf{x}}_{0|t}) = \underbrace{\frac{\sqrt{\bar{\alpha}_{t-1}} \beta_t}{1 - \bar{\alpha}_t}}_{=: a_t} \widehat{\mathbf{x}}_{0|t} + \frac{\sqrt{\bar{\alpha}_t} (1 - \bar{\alpha}_{t-1})}{1 - \bar{\alpha}_t} \mathbf{x}_t.\tag{7}$$

**Damped correction( $\lambda_t$ ) and variance matching( $\gamma_t$ ).** Following the “project-and-correct” view, Wang *et al.* [62]

propose to parametrize and dampen the update weight  $1 \rightarrow \lambda_t$  for the data-fidelity (null-space) update, and adjust the diffusion noise by  $\sigma_t \rightarrow \gamma_t$ . This changes lines 4 and 5 of Algorithm 1 to the following:

$$\widehat{\mathbf{x}}_{0|t} = \mathbf{x}_{0|t} - \lambda_t \mathbf{A}^\dagger (\mathbf{A}\mathbf{x}_{0|t} - \mathbf{y}),\tag{8}$$

$$\mathbf{x}_{t-1} = \boldsymbol{\mu}_t(\mathbf{x}_t, \widehat{\mathbf{x}}_{0|t}) + \gamma_t \boldsymbol{\epsilon}_t, \quad \boldsymbol{\epsilon}_t \sim \mathcal{N}(\mathbf{0}, \mathbf{I}).\tag{9}$$

Since  $\widehat{\mathbf{x}}_{0|t}$  contains  $\mathbf{A}^\dagger \boldsymbol{\eta}$ , the sampling mean (7) injects an additional noise term  $a_t \lambda_t \mathbf{A}^\dagger \boldsymbol{\eta}$  with covariance  $a_t^2 \lambda_t^2 \sigma_y^2 \mathbf{A}^\dagger \mathbf{A}^*$ . For the simple linear operators used in the linear tasks selected, they are treated as isotropic and set  $\gamma_t$  to preserve the target posterior variance. The two principles that guide the adaptive calculation of the new parameters are as follows:

i) Variance should be preserved in each step  $t$ ,

$$\gamma_t^2 = \max(0, \sigma_t^2 - a_t^2 \lambda_t^2 \sigma_y^2).\tag{10}$$

ii)  $\lambda_t$  should be as close as possible to 1,

$$\lambda_t = \begin{cases} 1, & \sigma_t \geq a_t \sigma_y, \\ \frac{\sigma_t}{a_t \sigma_y}, & \sigma_t < a_t \sigma_y. \end{cases}\tag{11}$$

*Interpretation:*  $a_t$  is the coefficient on  $\widehat{\mathbf{x}}_{0|t}$  in the posterior mean,  $\lambda_t$  controls the strength of the fidelity (null-space) correction,  $\sigma_y$  is the measurement-noise std., and  $\gamma_t$  is the residual diffusion noise after accounting for injected measurement noise.

#### 7.2. Can this scheme extend to flow models?

Reframe equation 10 as  $\gamma_t^2 = \sigma_t^2 - (a_t \lambda_t \sigma_y)^2$  leads to the following condition for  $\gamma_t$ :

$$\gamma_t = \begin{cases} \sigma_t^2 - (a_t \sigma_y)^2, & \sigma_t \geq a_t \sigma_y, \\ 0, & \sigma_t < a_t \sigma_y. \end{cases}\tag{12}$$

Since flow models do not have a noise schedule  $\sigma_t$ , it is equivalent to setting  $\sigma_t = 0$ . This would imply the second case ( $\sigma_t < a_t \sigma_y$ ) of equations 11 and 12, leading to  $\gamma_t = 0$  and

$$\lambda_t = \frac{\sigma_t}{a_t \sigma_y} = 0.\tag{13}$$

Thus, in a flow model with no noise schedule  $\sigma_t \equiv 0$  the noise-aware formulation collapses to  $\gamma_t = 0$  and  $\lambda_t = 0$ —i.e., no fidelity correction. Moreover, the core principle of “preserving the variance in each timestep  $t$ ” does not apply, since a flow model does not have an inherent variance

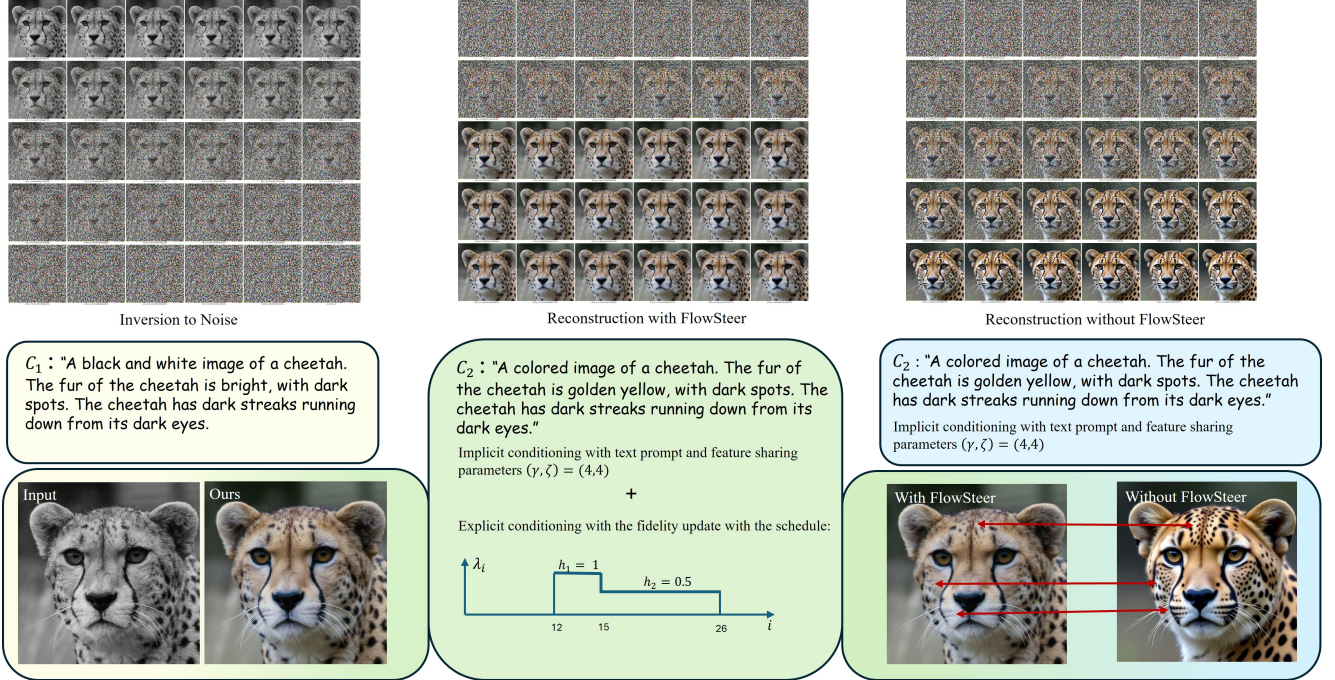


Figure 9. FlowSteer- an overview. Left: The input degraded image is inverted to noise. The source prompt  $C_1$  guides the inversion flow path. Middle: The FlowSteer reconstruction path- which is conditioned by the target caption  $C_2$ , feature sharing parametrized by  $(\gamma, \zeta)$ , and the fidelity update scheduled by the  $\lambda_i$ . Right: The FlowSteer output is compared against our baseline flow model without FlowSteer. The implicit conditioning without FlowSteer generates unnecessary hallucinations. (Zoom in for a better view).

schedule through  $\sigma_t$ . This shows that the diffusion-style noise-robust update does not transfer directly to flows. Empirically, we find that fidelity updates in flow models are sensitive to measurement noise and, if used at all, must be applied sparingly with careful, task-dependent tuning.

## 8. More Details on the Flow Model

FlowSteer, and all related baselines were implemented on an NVIDIA A100 GPU with VRAM 80GB. Resources were only required for model inference.

### 8.1. Feature sharing

The Flux-dev [31] model is our base-line image editing model, that we adapt for image restoration. Both the inversion path and the reconstruction path has  $N = 30$  steps. The velocity prediction  $v_\theta(\cdot)$  in each step is modeled through a Diffusion Transformer (DiT) [14] block. The diffusion transformer has “double-block” layers and “single block” layers, out of which the “single block” layers are used for feature sharing. The attention maps that are calculated in the last  $\zeta$  inversion steps (input to noise) and correspond to the first  $\zeta$  reconstruction steps (noise to image). During reconstruction, the cached attention maps are used for the first  $\zeta$  steps, creating an implicit conditioning that the

reconstructed image should preserve some qualities of the original image. There are similar approaches in literature of caching attention maps or just the Values or Key-Query pairs to drive an edited image/video to be faithful to an input image. [5, 6, 15, 18, 19, 27, 33, 42, 60, 66]. In our design, we cache the complete attention map. However, after experimenting with different feature sharing schemes and grid searches through hyper-parameters as described in section 3, we find that such implicit conditioning is insufficient for enforcing the pixel-level fidelity required for image restoration tasks.

### 8.2. Text prompts

As described in section 3, there are two types of prompts that implicitly condition the flow field. During inversion, the source prompt  $C_1$  is used to describe the degraded image. During reconstruction, the target prompt  $C_2$  is used to describe the target image features. The prompts are manually selected by the user. The table 4 shows the sample prompts used for each of the restoration tasks.

## 9. Details on the Degradation Models

**Colorization.** The forward operator  $\mathbf{A}$  maps RGB to an achromatic image by averaging channels and repeating the

result across three channels. For  $\mathbf{x} \in \mathbb{R}^{3 \times H \times W}$  and pixel  $p$ ,

$$(\mathbf{Ax})_c(p) = \frac{1}{3} \sum_{k=1}^3 x_k(p), \quad c \in \{1, 2, 3\}.$$

The Moore–Penrose pseudoinverse coincides with  $\mathbf{A}$ , i.e.

$$\mathbf{A}^\dagger \mathbf{y} = \mathcal{R} \left( \frac{1}{3} \sum_{k=1}^3 y_k \right),$$

where  $\mathcal{R}(\cdot)$  replicates a single channel three times. Hence, for any  $\mathbf{y} \in \text{range}(\mathbf{A})$  (three identical channels),  $\mathbf{A}^\dagger \mathbf{y} = \mathbf{y}$  and  $\mathbf{AA}^\dagger = \mathbf{A}$ .

**Deblurring.** The forward operator is a circular Gaussian blur  $\mathbf{A}$  (convolution with kernel  $h$ ). We use the Tikhonov-regularized (Wiener-type) pseudoinverse parameterized by  $\lambda_w$ ,

$$\mathbf{A}_{\lambda_w}^\dagger \triangleq (\mathbf{A}^* \mathbf{A} + \lambda_w \mathbf{I})^{-1} \mathbf{A}^*,$$

where  $\mathbf{A}^*$  denotes the adjoint of  $\mathbf{A}$ . We set  $\lambda_w = 0.1$  in all our experiments. The forward model can be implemented using Fourier transforms as  $\mathcal{F}\{\mathbf{y}\} = \mathcal{F}\{h\} \mathcal{F}\{\mathbf{x}\}$ , (or equivalently, as the convolution  $\mathbf{y} = h * \mathbf{x}$ ). The inversion is implemented in python code in the following form,

$$\mathbf{A}_{\lambda_w}^\dagger \mathbf{y} = \mathcal{F}^{-1} \left[ \frac{\overline{\mathcal{F}\{h\}}}{|\mathcal{F}\{h\}|^2 + \lambda_w} \mathcal{F}\{\mathbf{y}\} \right].$$

$\overline{\mathcal{F}\{h\}}$  is the element-wise complex conjugate of  $\mathcal{F}\{h\}$ . For a real, symmetric Gaussian kernel  $h$ ,  $\overline{\mathcal{F}\{h\}} = \mathcal{F}\{h\}$ .

**Super-resolution ( $\times 4$ ).** The forward operator  $\mathbf{A}$  down-samples an RGB image by average-pooling over non-overlapping  $4 \times 4$  blocks (per channel) and decimating by a factor of 4 along height and width:  $\mathbf{y} = \mathbf{Ax} \in \mathbb{R}^{3 \times H/4 \times W/4}$  with

$$y_c(u, v) = \frac{1}{16} \sum_{i,j=0}^3 x_c(4u+i, 4v+j).$$

As a practical pseudo-inverse we use a right-inverse that restores the original spatial size by *patch replication* (nearest-neighbor up-sampling):

$$(\mathbf{A}^\dagger \mathbf{y})_c(i, j) = \mathbf{y}_c(\lfloor i/4 \rfloor, \lfloor j/4 \rfloor),$$

such that  $\mathbf{AA}^\dagger = \mathbf{I}$  on  $\mathbb{R}^{3 \times H/4 \times W/4}$ .

**Denoising.** We model denoising with the identity forward operator  $\mathbf{A} = \mathbf{I}$ , so the measurement is simply  $\mathbf{y} = \mathbf{Ax} + \boldsymbol{\eta} = \mathbf{x} + \boldsymbol{\eta}$ . Because  $\mathbf{I}$  is self-adjoint and full-rank, its Moore–Penrose pseudoinverse is itself:  $\mathbf{A}^\dagger = \mathbf{I}$ .

## 10. Design Details for $\{\lambda_i\}$

### 10.1. A Two-Step Schedule

In section 5.3 we describe the effect of the schedule  $\{\lambda_i\}$ . Empirically we observe that a single step-design as mentioned in table 2 (left) is sufficient for general reconstructions. However, the reconstruction quality can be improved by having a scheduler that gradually reduces the strength of the fidelity update. This empirical observation is shown in table 2 (right).

The following is the python-style implementation of a two-step scheduler, with the parameters  $i_{\text{start}}, i_{\text{step}}, i_{\text{end}}, h_1, h_2$ . Between  $i_{\text{start}}, i_{\text{step}}$  the value of  $\lambda_i$  is  $h_1$ , and between  $i_{\text{step}}, i_{\text{end}}$  the value of  $\lambda_i$  is  $h_2$ .

Listing 1. Step-shaped  $\lambda_i$  schedule used in SteerFlow.

```

1 def make_lambda_step_schedule(
2     timesteps,
3     *, start, step, end,
4     h_1=1.0, h_2=0.5,
5     final_pad=1,
6 ):
7     N = len(timesteps) - 1
8     lam = np.zeros(N, dtype=np.float32)
9     if N <= 0:
10         return lam
11
12     i_0 = to_index(start, N)
13     i_1 = to_index(step, N)
14     # make end exclusive
15     i_2 = to_index(end, N) + 1
16
17     # order & clamp
18     i_start, i_step = min(i_0, i_1), max(i_0, i_1)
19     i_step, i_end = min(i_1, i_2), max(i_1, i_2)
20     i_start = np.clip(i_start, 0, N)
21     i_step = np.clip(i_step, 0, N)
22     i_end = np.clip(i_end, 0, N)
23
24     if i_start < i_step:
25         lam[i_start:i_step] = h_1
26     if i_step < i_end:
27         lam[i_step:i_end] = h_2
28
29     if 0 < final_pad < N:
30         lam[-final_pad:] = 0.0
31
32     # keep a peak=1 if padding nuked it
33     if lam.max() <= 0 and N - final_pad - 1 >= 0:
34         lam[N - final_pad - 1] = 1.0
35     else:
36         lam /= max(1.0, float(lam.max()))
37     return lam

```

### 10.2. Effect of the Fidelity update

The effect of the fidelity update is visually shown in the figures 10 and 11. If the update is started too late ( $i_{\text{start}}$  is too late), then the reconstruction will have artifacts from

the hallucinated details. (figure 10). If the update is started too early ( $i_{\text{start}}$  is too early), then the desired level of hallucinations (such as rich colors for colorization) have not yet formed. This makes the reconstruction have over smoothness, and loose color and texture details. (figure 11).

### 10.3. Final padding

A final padding parameter is added to enforce that at least a few steps of the reconstruction path does not end with a fidelity update. This is another empirical design decision, where we observe that having some steps without fidelity updates helps to smoothen out some of the noise artifacts. However, if the final padding is too high, the image can get oversmoothed. This is effectively the same as having a fidelity update too early on in the reconstruction path, as shown in figure 11.

## 11. Limitations and Future Directions

### 11.1. Empirical schedule

The Flow Steer schedule recommendations are given through empirical fine-tuning. For the four restoration tasks together, we recommend a one-step schedule in Table 2(left). For each task separately, we recommend a two-step schedule in Table 2(right). Even with this task-specific schedule recommendation, there are cases where the schedule does not work for every image in the dataset. This can be seen in some of the failure cases for the current Steer-Flow scheme as shown in Figure 12.

A future directions would be to extend this schedule to be adaptable for each individual image, so that manual tuning can be avoided. The key is to estimate the noise injected by the fidelity update and trigger the update at the step whose model noise budget best matches it, while adjusting the update strength  $\{\lambda_t\}$  accordingly. This would lead to an image-adaptive scheduler, and will not have to depend on heuristics.

### 11.2. Artifacts from explicit conditioning

The explicit conditioning of FlowSteer relies on Pseudoinverse operators. This has the inherent limitation of introducing artifacts, such as shown in figure 13. Apart from the noisy artifacts described above, there are instances of blocking-artifacts from the upsampling operation in super-resolution, and ringing-artifacts from the Wiener filter in deblurring.

## 12. More Visual Results

### 12.1. More visual results on restoration tasks

More images on the restoration tasks, highlighting that we preserve both pixel-level fidelity and rich perceptual quality. Zoom in and highlight differences. Refer figure 15.

### 12.2. Plug-and-Play(PnP) on pre-trained Flow models

We recreate the results of PnP-Flow [36] to verify if a Plug-and-play type algorithm can achieve visually appealing images after image restoration. It was observed that it performs well only when the underlying model is the provided model from the authors, which is specifically trained for the class of images being tested. For example, with the pre-trained flow model (which has been trained on a cat dataset) it gives plausible results on cat images. However, when flux-dev [31] (which is trained on a much broader class of data) is used as the underlying flow model, the Plug-and-play method fails to converge to a plausible reconstruction. A grid search was run to select the hyper-parameters of the PnP algorithm and the values:  $(\alpha, \gamma, \eta_{dn}) = (0.3, 0.8, 0.3)$  were selected. This is demonstrated in Figure 14.

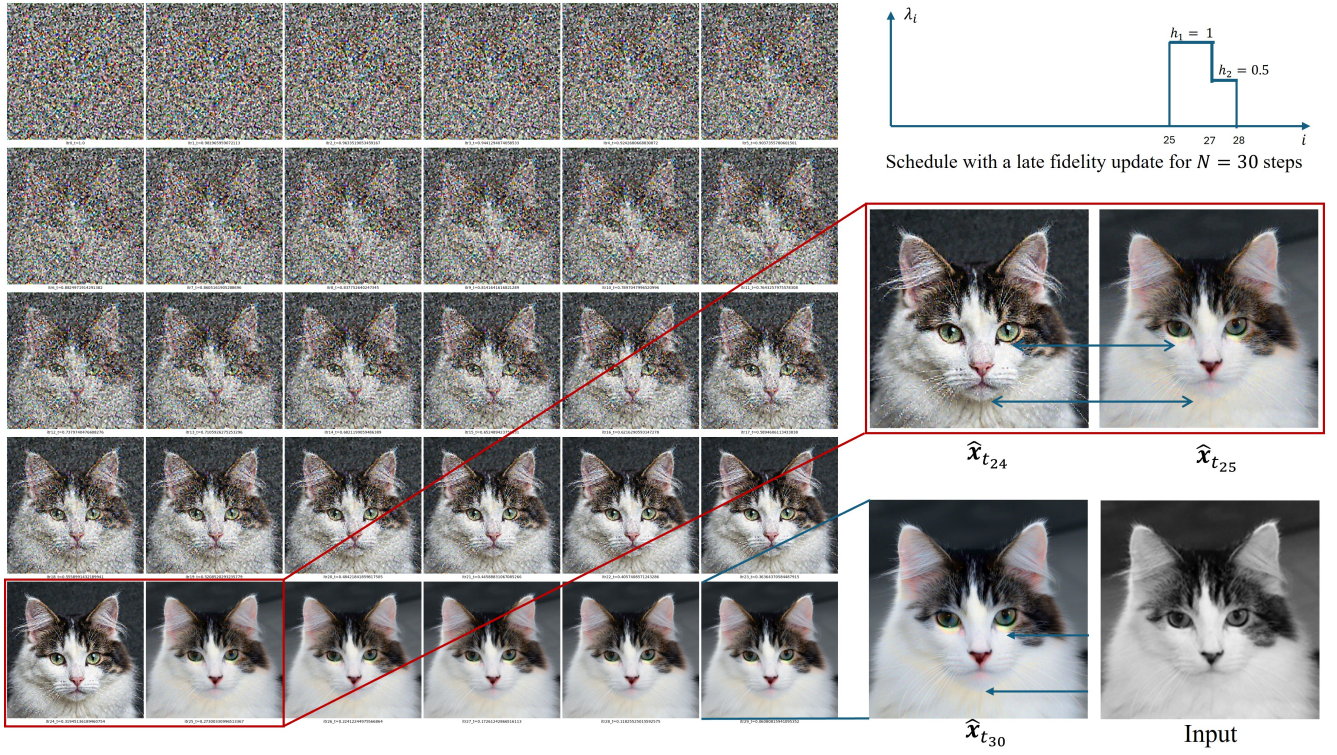


Figure 10. Visualising the reconstruction path with the fidelity update being late. Before the fidelity update has been applied ( $\hat{x}_{t_{24}}$ ), the flux model has already hallucinated fine textures and colors. Immediately after activation ( $\hat{x}_{t_{25}}$ ), the fidelity update steers the path toward the measurement. However, some residual artifacts persist in the final reconstruction.

Type	#	Source prompt $C_1$	Target prompt $C_2$
<i>Colorization</i>			
Pets	1	A black and white image of a cat. The cat is white with black patches. The background is dark. The nose of the cat is pink. The eyes of the cat are green.	A colorful image of a cat. The cat is white with black patches. The background is dark. The nose of the cat is pink. The eyes of the cat are green.
Wild	2	A black and white image of a cheetah. The fur of the leopard is bright, with dark spots. The leopard has dark streaks running down from its dark eyes.	A colored image of a cheetah. The fur of the leopard is golden yellow, with dark spots. The leopard has dark streaks running down from its dark eyes.
Wild	3	A black and white image of a fox. The fox has brown fur with white streaks. The nose of the fox is black. The eyes of the fox are dark brown.	A colorful image of a fox. The fox has brown fur with white streaks. The nose of the fox is black. The eyes of the fox are dark brown.
Humans	4	A black and white image of a man.	A colorful image of a man. The man has black eyes.
<i>Deblurring</i>			
Pets	1	A blurred image of a cat. The cat has white fur with black spots.	A sharp image of a cat. The cat has white fur with black spots. Highly detailed, taken using a Canon EOS R camera, hyper detailed photo-realistic maximum detail.
Wild	2	A blurred image of a lion. The lion has golden colored fur and dark brown eyes.	A sharp image of a lion. The lion has golden colored fur and dark brown eyes. Highly detailed, taken using a Canon EOS R camera, hyper detailed photo-realistic maximum detail.
Wild	3	A blurred image of a leopard. The leopard has brown fur and black patches.	A sharp image of a leopard. The leopard has brown fur and black patches. Highly detailed, taken using a Canon EOS R camera, hyper detailed photo-realistic maximum detail.
Humans	4	A blurred image of a man.	A sharp image of a man. Highly detailed, taken using a Canon EOS R camera, hyper detailed photo-realistic maximum detail.
<i>Super-resolution</i>			
Pets	1	A low resolution image of a dog. The dog is brown with white patches.	A sharp, high resolution image of a dog. The dog is brown with white patches. Highly detailed, taken using a Canon EOS R camera, hyper detailed photo-realistic maximum detail.
Wild	2	A low resolution image of a lion. The lion has golden colored fur and dark brown eyes.	A sharp, high resolution image of a lion. The lion has golden colored fur and dark brown eyes. Highly detailed, taken using a Canon EOS R camera, hyper detailed photo-realistic maximum detail.
Humans	3	A low resolution image of a woman.	A sharp, high resolution image of a woman. Highly detailed, taken using a Canon EOS R camera, hyper detailed photo-realistic maximum detail.
<i>Denoising</i>			
Pets	1	A noisy image of a dog. The dog is brown with white patches.	A clean, noise free image of a dog. The dog is brown with white patches. Highly detailed, taken using a Canon EOS R camera, hyper detailed photo-realistic maximum detail. There are no RGB noise artifacts.
Wild	2	A noisy image of a cheetah. The fur of the cheetah is bright, with dark spots. The cheetah has dark streaks running down from its dark eyes.	A clean, noise free image of a cheetah. The fur of the cheetah is bright, with dark spots. The cheetah has dark streaks running down from its dark eyes. Highly detailed, taken using a Canon EOS R camera, hyper detailed photo-realistic maximum detail. There are no RGB noise artifacts.
Human	3	A noisy image of a man.	A clean, noise free image of a man. Highly detailed, taken using a Canon EOS R camera, hyper detailed photo-realistic maximum detail. There are no RGB noise artifacts.

Table 4. Sample prompt pairs per task. “Source” describes the input (e.g., grayscale, low-res, noisy, blurred); “Target” describes the intended restored image that is used to implicitly steer the flux model.

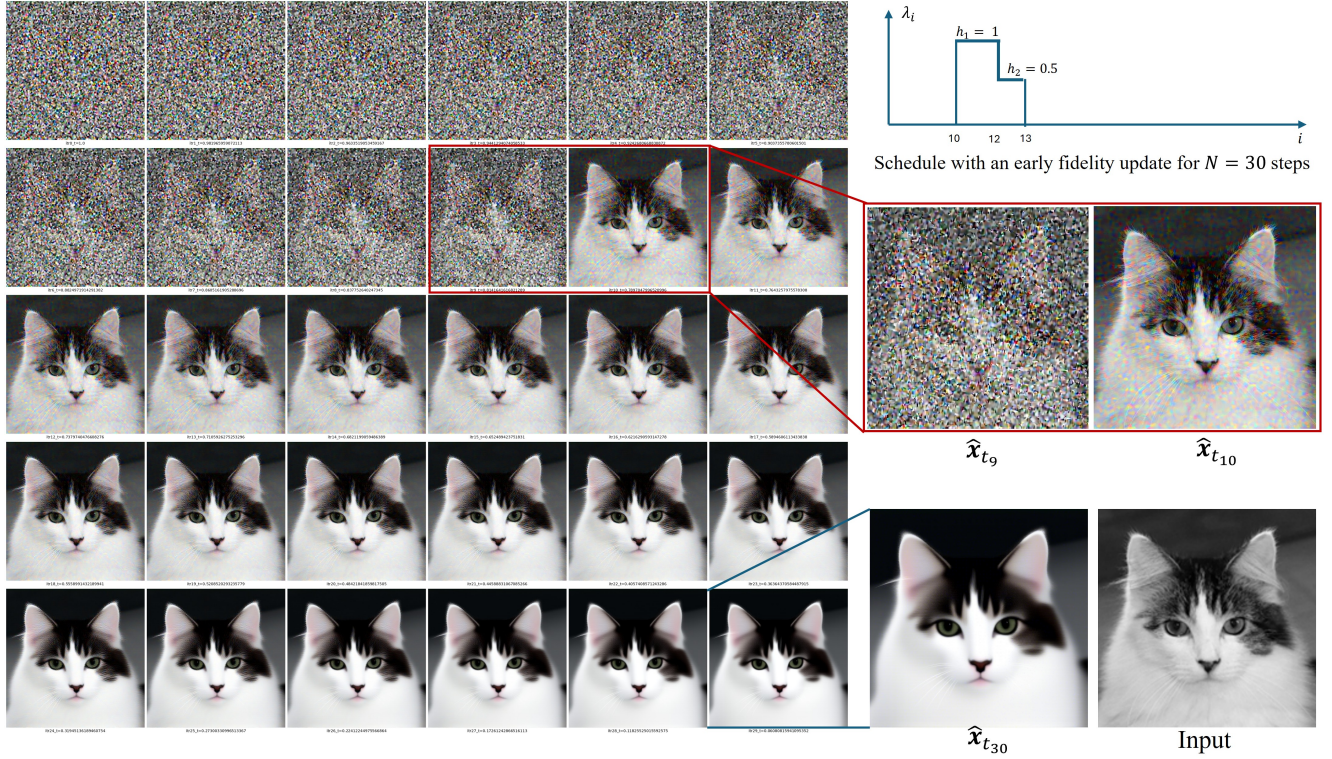


Figure 11. Visualising the reconstruction path with the fidelity update being early. Before the fidelity update has been applied ( $\hat{x}_{t_9}$ ), the flux model has not completely formed the color palette and textures. The fidelity update conditions the path to have less color ( $\hat{x}_{t_{10}}$ ), and the large number of steps without the fidelity update over smoothens the result. The same effect will be seen when a higher number of flux steps are padded at the end of the schedule, as described in Section 10.3.

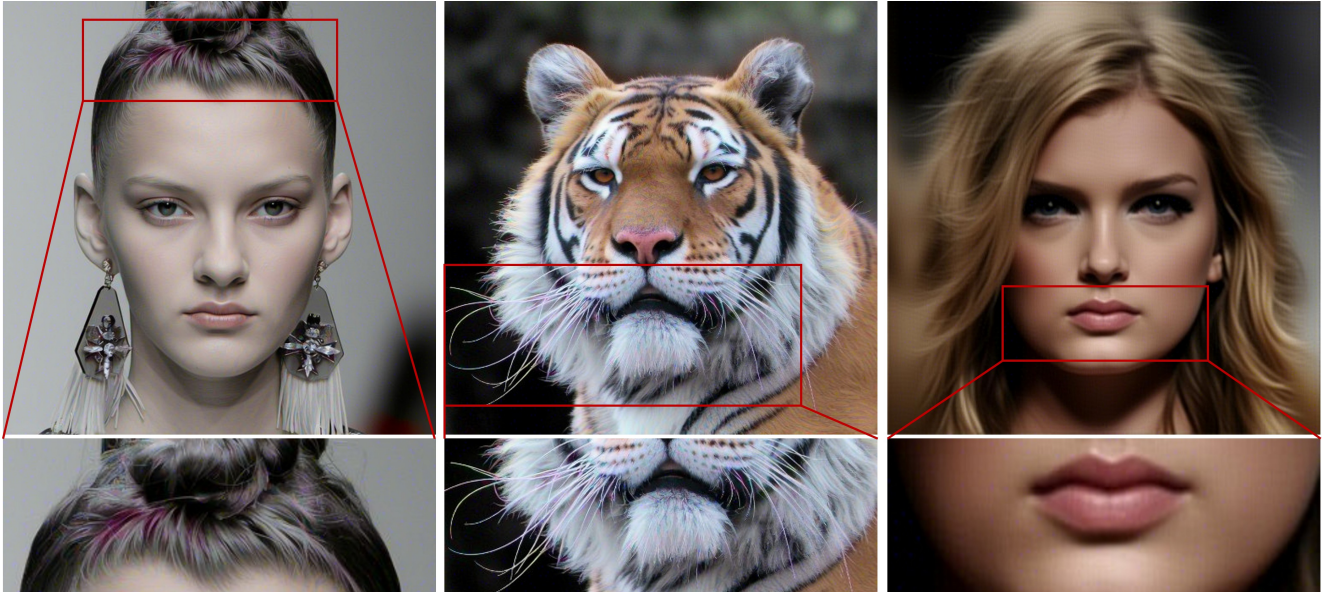


Figure 12. Noise artifacts are seen in some of the final reconstructed image with the two-step scheduler. The restoration tasks corresponding to these images are colorization (left and center) and deblurring (right). Fine tuning the scheduler on a per-image basis may reduce these artifacts as discussed in Section 11. Zoom in to clearly see the noise artifacts in some pixels.

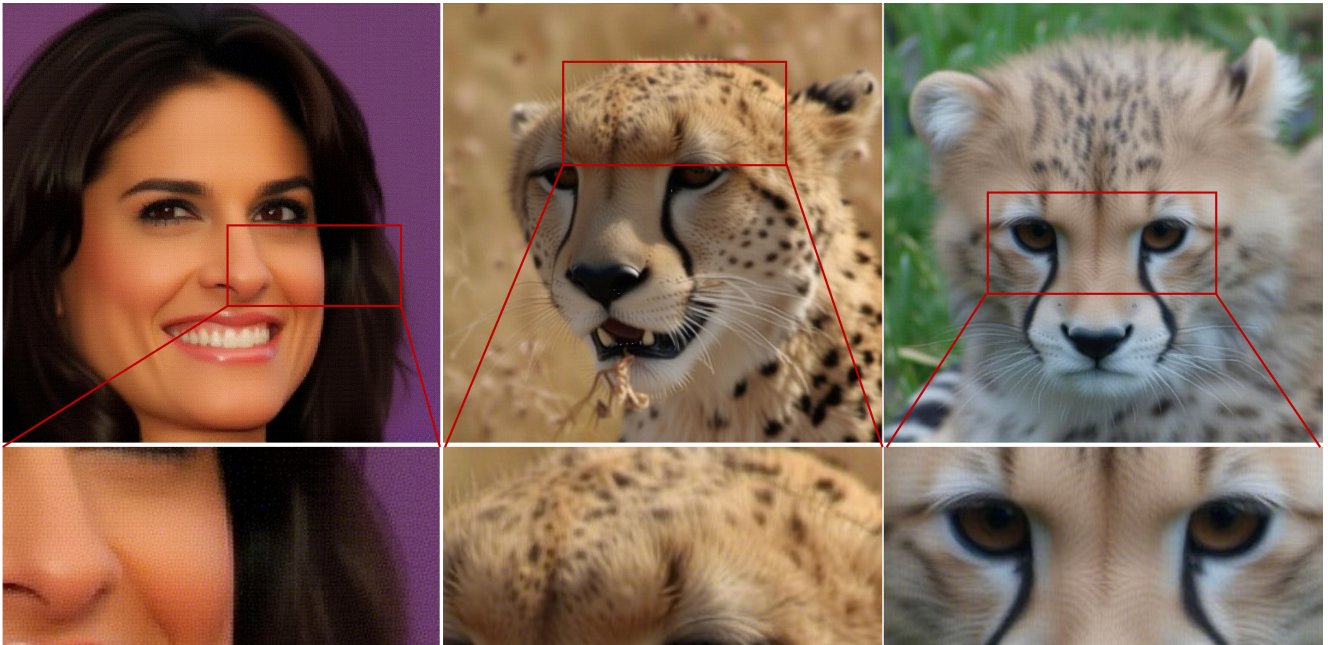


Figure 13. Artifacts resulting from Pseudo-inverse operators in FlowSteer as discussed in Section 11. Blocking artifacts affect edges in super-resolution(left). The Weiner filter creates ringing effects in deblurring(center and right). Zoom in to clearly see the artifacts.



Figure 14. Plug and play approach on different types of flow models. Although it produces plausible results on a flow model trained on cats(left), it does poorly when implemented on a flow model trained on other general data. This is described in Section 12.



Figure 15. More qualitative comparisons of flow-based methods against FlowSteer. The restoration models in columns 2-4 have undesirable artifacts such as excessive blur. The image editing baseline in column 5 has poor fidelity. FlowSteer achieves better pixel-level fidelity, while generating visually appealing details. Zoom in for better comparisons.

**Acknowledgements:** We are thankful for Mykhailo Tsysin and Yu Yuan for the helpful discussions.

## References

- [1] Michael S Albergo, Nicholas M Boffi, and Eric Vanden-Eijnden. Stochastic interpolants: A unifying framework for flows and diffusions. *arXiv preprint arXiv:2303.08797*, 2023. 1
- [2] Omri Avrahami, Dani Lischinski, and Ohad Fried. Blended diffusion for text-driven editing of natural images. In *Proceedings of the IEEE/CVF Conference on Computer Vision and Pattern Recognition (CVPR)*, pages 18208–18218, 2022. 1
- [3] Stephen Batifol, Andreas Blattmann, Frederic Boesel, Saksham Consul, Cyril Diagne, Tim Dockhorn, Jack English, Zion English, Patrick Esser, Sumith Kulal, et al. Flux. 1 kontext: Flow matching for in-context image generation and editing in latent space. *arXiv e-prints*, pages arXiv–2506, 2025. 2
- [4] Heli Ben-Hamu, Omri Puny, Itai Gat, Brian Karrer, Uriel Singer, and Yaron Lipman. D-flow: Differentiating through flows for controlled generation. *arXiv preprint arXiv:2402.14017*, 2024. 3, 6, 7, 8, 10
- [5] Mingdeng Cao, Xintao Wang, Zhongang Qi, Ying Shan, Xiaohu Qie, and Yinqiang Zheng. Masactrl: Tuning-free mutual self-attention control for consistent image synthesis and editing. In *IEEE/CVF International Conference on Computer Vision (ICCV)*, pages 22560–22570, 2023. 2
- [6] Duygu Ceylan, Chun-Hao P Huang, and Niloy J Mitra. Pix2video: Video editing using image diffusion. In *IEEE/CVF International Conference on Computer Vision (ICCV)*, pages 23206–23217, 2023. 2
- [7] Jooyoung Choi, Sungwon Kim, Yonghyun Jeong, Youngjune Gwon, and Sungroh Yoon. Ilvr: Conditioning method for denoising diffusion probabilistic models. *2021 IEEE/CVF International Conference on Computer Vision (ICCV)*, pages 14347–14356, 2021. 2
- [8] Yunje Choi, Youngjung Uh, Jaejun Yoo, and Jung-Woo Ha. Stargan v2: Diverse image synthesis for multiple domains. In *Proceedings of the IEEE/CVF Conference on Computer Vision and Pattern Recognition (CVPR)*, pages 8188–8197, 2020. 6
- [9] Hyungjin Chung, Jeongsol Kim, Michael T Mccann, Marc L Klasky, and Jong Chul Ye. Diffusion posterior sampling for general noisy inverse problems. *arXiv preprint arXiv:2209.14687*, 2022. 1, 2
- [10] Yusuf Dalva, Kavana Venkatesh, and Pinar Yanardag. Fluxspace: Disentangled semantic editing in rectified flow models. In *Proceedings of the IEEE/CVF Conference on Computer Vision and Pattern Recognition (CVPR)*, pages 13083–13092, 2025. 3
- [11] Yingying Deng, Xiangyu He, Changwang Mei, Peisong Wang, and Fan Tang. Fireflow: Fast inversion of rectified flow for image semantic editing. *arXiv preprint arXiv:2412.07517*, 2024. 3
- [12] Prafulla Dhariwal and Alex Nichol. Diffusion models beat gans on image synthesis. In *Advances in Neural Information Processing Systems*, 2021. 1, 7
- [13] Prafulla Dhariwal and Alex Nichol. guided-diffusion. <https://github.com/openai/guided-diffusion>, 2021. GitHub repository. 7, 8
- [14] Patrick Esser, Sumith Kulal, Andreas Blattmann, Rahim Entezari, Jonas Müller, Harry Saini, Yam Levi, Dominik Lorenz, Axel Sauer, Frederic Boesel, et al. Scaling rectified flow transformers for high-resolution image synthesis. In *Forty-first international conference on machine learning*, 2024. 2
- [15] Michal Geyer, Omer Bar-Tal, Shai Bagon, and Tali Dekel. Tokenflow: Consistent diffusion features for consistent video editing. *arXiv preprint arXiv:2307.10373*, 2023. 2
- [16] Rafael C. Gonzalez and Richard E. Woods. *Digital Image Processing*. Pearson, 4 edition, 2018. 6
- [17] Per Christian Hansen, James G. Nagy, and Dianne P. O’Leary. *Deblurring Images: Matrices, Spectra, and Filtering*. SIAM, 2006. 6
- [18] Amir Hertz, Ron Mokady, Jay Tenenbaum, Kfir Aberman, Yael Pritch, and Daniel Cohen-Or. Prompt-to-prompt image editing with cross attention control. *The Eleventh International Conference on Learning Representations (ICLR)*, 2023. 1, 6, 2
- [19] Amir Hertz, Andrey Voynov, Shlomi Fruchter, and Daniel Cohen-Or. Style aligned image generation via shared attention. In *Proceedings of the IEEE/CVF Conference on Computer Vision and Pattern Recognition (CVPR)*, pages 4775–4785, 2024. 2
- [20] Jonathan Ho and Tim Salimans. Classifier-free diffusion guidance, 2021. 3, 4
- [21] Jonathan Ho, Ajay Jain, and Pieter Abbeel. Denoising diffusion probabilistic models. In *Advances in Neural Information Processing Systems*, 2020. 1, 2
- [22] Guanlong Jiao, Biqing Huang, Kuan-Chieh Wang, and Renjie Liao. Unedit-flow: Unleashing inversion and editing in the era of flow models. *arXiv preprint arXiv:2504.13109*, 2025. 3
- [23] Tero Karras, Timo Aila, Samuli Laine, and Jaakko Lehtinen. Progressive growing of gans for improved quality, stability, and variation. *arXiv preprint arXiv:1710.10196*, 2017. 6
- [24] Bahjat Kavar, Gregory Vaksman, and Michael Elad. Snips: Solving noisy inverse problems stochastically. *Advances in Neural Information Processing Systems*, 34:21757–21769, 2021. 2
- [25] Bahjat Kavar, Michael Elad, Stefano Ermon, and Jiaming Song. Denoising diffusion restoration models. *Advances in Neural Information Processing Systems*, 35:23593–23606, 2022. 1, 2
- [26] Jeongsol Kim, Yeobin Hong, Jonghyun Park, and Jong Chul Ye. Flowalign: Trajectory-regularized, inversion-free flow-based image editing. *arXiv preprint arXiv:2505.23145*, 2025. 2
- [27] Jimyeong Kim, Jungwon Park, Yeji Song, Nojun Kwak, and Wonjong Rhee. Reflex: Text-guided editing of real images in rectified flow via mid-step feature extraction and attention

- adaptation. In *Proceedings of the IEEE/CVF International Conference on Computer Vision (ICCV)*, 2025. 2
- [28] Diederik P. Kingma and Max Welling. Auto-encoding variational bayes. In *International Conference on Learning Representations (ICLR)*, 2014. 4
- [29] Dehong Kong, Fan Li, Zhixin Wang, Jiaqi Xu, Renjing Pei, Wenbo Li, and Wenqi Ren. Dual prompting image restoration with diffusion transformers. In *Proceedings of the IEEE/CVF Conference on Computer Vision and Pattern Recognition (CVPR)*, pages 12809–12819, 2025. 2
- [30] Vladimir Kulikov, Matan Kleiner, Inbar Huberman-Spiegelglas, and Tomer Michaeli. Flowedit: Inversion-free text-based editing using pre-trained flow models. In *Proceedings of the IEEE/CVF International Conference on Computer Vision (ICCV)*, pages 19721–19730, 2025. 2
- [31] Black Forest Labs. FLUX. <https://github.com/black-forest-labs/flux>, 2024. 2, 3, 4, 5
- [32] Yaron Lipman, Ricky TQ Chen, Heli Ben-Hamu, Maximilian Nickel, and Matt Le. Flow matching for generative modeling. *arXiv preprint arXiv:2210.02747*, 2022. 2
- [33] Shaoteng Liu, Yuechen Zhang, Wenbo Li, Zhe Lin, and Jiaya Jia. Video-p2p: Video editing with cross-attention control. In *Proceedings of the IEEE/CVF Conference on Computer Vision and Pattern Recognition (CVPR)*, pages 8599–8608, 2024. 2
- [34] Xingchao Liu, Chengyue Gong, and Qiang Liu. Flow straight and fast: Learning to generate and transfer data with rectified flow. *arXiv preprint arXiv:2209.03003*, 2022. 2
- [35] Ziwei Liu, Ping Luo, Xiaogang Wang, and Xiaoou Tang. Deep learning face attributes in the wild. In *Proceedings of the IEEE International Conference on Computer Vision (ICCV)*, pages 3730–3738, 2015. 6
- [36] Ségolène Martin, Anne Gagneux, Paul Hagemann, and Gabriele Steidl. Pnp-flow: Plug-and-play image restoration with flow matching. *arXiv preprint arXiv:2410.02423*, 2024. 2, 3, 6, 7, 8, 4, 10
- [37] Chenlin Meng, Yutong He, Yang Song, Jiaming Song, Jianjun Wu, Jun-Yan Zhu, and Stefano Ermon. SDEdit: Guided image synthesis and editing with stochastic differential equations. In *International Conference on Learning Representations (ICLR)*, 2022. 1, 2
- [38] Chong Mou, Xintao Wang, Liangbin Xie, Yanze Wu, Jian Zhang, Zhongang Qi, and Ying Shan. T2i-adapter: Learning adapters to dig out more controllable ability for text-to-image diffusion models. In *Proceedings of the AAAI conference on artificial intelligence*, pages 4296–4304, 2024. 1
- [39] Alexander Quinn Nichol and Prafulla Dhariwal. Improved denoising diffusion probabilistic models. In *International conference on machine learning*, pages 8162–8171. PMLR, 2021. 2
- [40] Yong-Hyun Park, Mingi Kwon, Jaewoong Choi, Junghyo Jo, and Youngjung Uh. Understanding the latent space of diffusion models through the lens of riemannian geometry. *Advances in Neural Information Processing Systems*, 36: 24129–24142, 2023. 6
- [41] Ashwini Pople, Matthew J. Muckley, Ricky T. Q. Chen, and Brian Karrer. Training-free linear image inverses via flows. *Transactions on Machine Learning Research (TMLR)*, 2024. Often referred to as OT-ODE. 6, 8
- [42] Chenyang Qi, Xiaodong Cun, Yong Zhang, Chenyang Lei, Xintao Wang, Ying Shan, and Qifeng Chen. Fatezero: Fusing attentions for zero-shot text-based video editing. In *IEEE/CVF International Conference on Computer Vision (ICCV)*, pages 15932–15942, 2023. 2
- [43] Alec Radford, Jong Wook Kim, Chris Hallacy, Aditya Ramesh, Gabriel Goh, Sandhini Agarwal, Girish Sastry, Amanda Askell, Pamela Mishkin, Jack Clark, et al. Learning transferable visual models from natural language supervision. In *International conference on machine learning*, pages 8748–8763. PMLR, 2021. 6
- [44] Robin Rombach, Andreas Blattmann, Dominik Lorenz, Patrick Esser, and Björn Ommer. High-resolution image synthesis with latent diffusion models. In *Proceedings of the IEEE/CVF Conference on Computer Vision and Pattern Recognition (CVPR)*, pages 10684–10695, 2022. 1, 4
- [45] Litu Rout, Yujia Chen, Nataniel Ruiz, Constantine Caramanis, Sanjay Shakkottai, and Wen-Sheng Chu. Semantic image inversion and editing using rectified stochastic differential equations. In *The Thirteenth International Conference on Learning Representations (ICLR)*, 2025. 1, 3
- [46] Chitwan Saharia, Jonathan Ho, William Chan, Tim Salimans, David J Fleet, and Mohammad Norouzi. Image super-resolution via iterative refinement. *IEEE transactions on pattern analysis and machine intelligence*, 45(4):4713–4726, 2022. 1
- [47] Ketan Suhaas Saichandran, Xavier Thomas, Prakhara Kaushik, and Deepti Ghadiyaram. Progressive prompt detailing for improved alignment in text-to-image generative models. In *Proceedings of the IEEE/CVF Conference on Computer Vision and Pattern Recognition (CVPR) Workshops*, 2025. 6
- [48] Axel Sauer, Frederic Boesel, Tim Dockhorn, Andreas Blattmann, Patrick Esser, and Robin Rombach. Fast high-resolution image synthesis with latent adversarial diffusion distillation. In *SIGGRAPH Asia 2024 Conference Papers*, pages 1–11, 2024. 2
- [49] Johannes Schusterbauer, Ming Gui, Frank Fundel, and Björn Ommer. Diff2flow: Training flow matching models via diffusion model alignment. In *Proceedings of the IEEE/CVF Conference on Computer Vision and Pattern Recognition (CVPR)*, pages 28347–28357, 2025. 2
- [50] Andy Shih, Suneel Belkhale, Stefano Ermon, Dorsa Sadigh, and Nima Anari. Parallel sampling of diffusion models. *Advances in Neural Information Processing Systems*, 36:4263–4276, 2023. 1
- [51] Bowen Song, Soo Min Kwon, Zecheng Zhang, Xinyu Hu, Qing Qu, and Liye Shen. Solving inverse problems with latent diffusion models via hard data consistency. *The Eleventh International Conference on Learning Representations (ICLR)*, 2024. 1
- [52] Jiaming Song, Chenlin Meng, and Stefano Ermon. Denoising diffusion implicit models. *arXiv:2010.02502*, 2020. 1, 2
- [53] Yang Song, Jascha Sohl-Dickstein, Diederik P Kingma, Abhishek Kumar, Stefano Ermon, and Ben Poole. Score-based

- generative modeling through stochastic differential equations. *arXiv preprint arXiv:2011.13456*, 2020. 2
- [54] Stability.ai. Stable Diffusion 3. <https://stability.ai/news/stable-diffusion-3-research-paper>, 2024. 2
- [55] Narek Tumanyan, Michal Geyer, Shai Bagon, and Tali Dekel. Plug-and-play diffusion features for text-driven image-to-image translation. In *Proceedings of the IEEE/CVF Conference on Computer Vision and Pattern Recognition (CVPR)*, pages 1921–1930, 2023. 1
- [56] Narek Tumanyan, Michal Geyer, Shai Bagon, and Tali Dekel. Plug-and-play diffusion features for text-driven image-to-image translation. In *Proceedings of the IEEE/CVF Conference on Computer Vision and Pattern Recognition (CVPR)*, pages 1921–1930, 2023. 1
- [57] Singanallur V Venkatakrishnan, Charles A Bouman, and Brendt Wohlberg. Plug-and-play priors for model based reconstruction. In *2013 IEEE global conference on signal and information processing*, pages 945–948. IEEE, 2013. 2
- [58] Bram Wallace, Akash Gokul, and Nikhil Naik. Edict: Exact diffusion inversion via coupled transformations. In *Proceedings of the IEEE/CVF Conference on Computer Vision and Pattern Recognition (CVPR)*, pages 22532–22541, 2023. 2
- [59] Chong Wang, Lanqing Guo, Zixuan Fu, Siyuan Yang, Hao Cheng, Alex C Kot, and Bihan Wen. Reconciling stochastic and deterministic strategies for zero-shot image restoration using diffusion model in dual. In *Proceedings of the IEEE/CVF Conference on Computer Vision and Pattern Recognition (CVPR)*, pages 23207–23216, 2025. 2
- [60] Jiangshan Wang, Junfu Pu, Zhongang Qi, Jiayi Guo, Yue Ma, Nisha Huang, Yuxin Chen, Xiu Li, and Ying Shan. Tam-ing rectified flow for inversion and editing. *arXiv preprint arXiv:2411.04746*, 2024. 2, 3, 6, 7, 8, 10
- [61] Siyuan Wang, Yuyao Yan, Xi Yang, Rui Zhang, Qiufeng Wang, Guangliang Cheng, and Kaizhu Huang. Point2pix-zero: Point-driven refined diffusion for multi-object image editing. *Pattern Recognition*, page 112041, 2025. 1
- [62] Yinhuai Wang, Jiwen Yu, and Jian Zhang. Zero-shot image restoration using denoising diffusion null-space model. *The Eleventh International Conference on Learning Representations (ICLR)*, 2023. 2, 6, 7, 8, 1
- [63] Binxin Yang, Shuyang Gu, Bo Zhang, Ting Zhang, Xuejin Chen, Xiaoyan Sun, Dong Chen, and Fang Wen. Paint by example: Exemplar-based image editing with diffusion models. In *Proceedings of the IEEE/CVF Conference on Computer Vision and Pattern Recognition (CVPR)*, pages 18381–18391, 2023. 1
- [64] Xiaofeng Yang, Cheng Chen, Xulei Yang, Fayao Liu, and Guosheng Lin. Text-to-image rectified flow as plug-and-play priors. *arXiv preprint arXiv:2406.03293*, 2024. 1, 3
- [65] Richard Zhang, Phillip Isola, Alexei A Efros, Eli Shechtman, and Oliver Wang. The unreasonable effectiveness of deep features as a perceptual metric. In *Proceedings of the IEEE/CVF Conference on Computer Vision and Pattern Recognition (CVPR)*, 2018. 6
- [66] Yuechen Zhang, Jinbo Xing, Eric Lo, and Jiaya Jia. Real-world image variation by aligning diffusion inversion chain. *Advances in Neural Information Processing Systems*, 36: 30641–30661, 2023. 2
- [67] Yasi Zhang, Peiyu Yu, Yaxuan Zhu, Yingshan Chang, Feng Gao, Ying Nian Wu, and Oscar Leong. Flow priors for linear inverse problems via iterative corrupted trajectory matching. *Advances in Neural Information Processing Systems*, 37:57389–57417, 2024. 3, 6, 7, 8, 10
- [68] Yuanzhi Zhu, Kai Zhang, Jingyun Liang, Jiezhong Cao, Bihan Wen, Radu Timofte, and Luc Van Gool. Denoising diffusion models for plug-and-play image restoration. In *Proceedings of the IEEE/CVF Conference on Computer Vision and Pattern Recognition (CVPR)*, pages 1219–1229, 2023. 2